Lasers Med Sci (2018) 33:123–134
https://doi.org/10.1007/s10103-017-2350-3

ORIGINAL ARTICLE

Microvascular imaging and monitoring of human oral cavity lesions in vivo by swept-source OCT-based angiography

Wei Wei[1] · **Woo June Choi**[1] · **Ruikang K. Wang**[1]

Received: 29 May 2017 / Accepted: 1 October 2017 / Published online: 16 October 2017

Abstract We report the development of optical coherence tomography- (OCT) based angiography (OCTA) to image blood flow within microcirculatory tissue beds in human oral cavity in vivo with a field of view at 10 mm × 10 mm. Three-dimensional (3D) structural and vascular images of labial mucosa tissue are obtained at a single 3D acquisition. Pathologic mucosal sites with mouth ulcers are examined using the OCT tomograms and angiograms, upon which to monitor the lesion healing process over a period of 2 weeks. Quantitative metrics of the capillary loop density within the lamina propria layer are evaluated, providing statistically significant difference between healthy and diseased conditions over time. Furthermore, tissue anatomy and vessel morphology of other susceptible sites to ulcer, such as tongue, alveolar mucosa, and labial frenulum, are also imaged to demonstrate the promise of the proposed method as a clinically useful tool for the diagnosis and monitoring of therapeutic treatment of oral tissue abnormalities.

Keywords Optical coherence tomography (OCT) · OCT angiography · Swept-source OCT · Oral cavity vasculature · Capillary loop density · Oral lesion

Introduction

Disease involving oral mucosa is one of the most common diseases worldwide, not only impairing digestive functions, but also threatening overall health. Taking oral cancer as an example, there is approximately 48,250 cases newly diagnosed in the USA and over 640,000 cases across the world in 2016 [1, 2]. Unfortunately, oral cancer in patients is mostly found at relatively later stage, leading to an average 5-year mortality rate of ~ 43% (the mortality rate largely increases from ~ 17 to ~ 62% when the oral cancer progresses from local stage to distant stage) [1]. Therefore, the detection of early stage cancerization plays an important role in preventing and combating oral cancers. Other oral diseases, although not directly life-threatening, can still cause heavy burden to both patients and healthcare system due to necessarily repeated check-up and treatment, amounting to the fourth most expensive disease in industrialized countries [2, 3]. Other systemic conditions, such as diabetes or vitamin deficiency, or the local effects of chronic tobacco or alcohol use can also give rise to physiologic alterations in the oral mucosa [4]. Clearly, there is an urgent need for cost-effective diagnostic tools that can be used to screen and diagnose oral abnormalities, analyze pathological changes, and monitor the lesion recovery.

Generally, clinical diagnosis of oral disease is made up of visual examination, tactile assessment, and invasive biopsy. Due to limited visual resolution and subjective criteria, physicians often have limited access to the detailed state of diseases, and consequently have difficulty in managing oral treatment at early stage. An endoscopic microscope may help improve the detectable resolution on mucosa surface [5, 6], but still cannot reach deeper structures/vasculatures involving worthy information about "where the disease from" and "how the disease will develop." Recent development of photoacoustic microscopy (PAM) shows promise in imaging tissue microvascular features in vivo [7]; however, the feasibility of PAM imaging of oral mucosa has yet to demonstrate.

Optical coherence tomography (OCT) [8–10] is attractive for non-invasive oral cavity imaging because of its high-

Wei Wei and Woo June Choi contributed equally to this work.

✉ Ruikang K. Wang
wangrk@uw.edu

[1] Department of Bioengineering, University of Washington, 3720 15th Ave NE, Seattle, WA 98195, USA

resolution, high-speed, and reasonable imaging depth [11–17]. The feasibility of OCT for imaging oral mucosa disorders in vivo has been reported by analyzing various physiological oral architectures, such as cross-sectional collagen morphology [18], distribution of dysplastic cells [19], and distribution of salivary glands [20]. Statistical differences were found in these assessments between diseased and normal tissues. Recently, wide-field oral tissues of 33 mm (length) × 4.7 mm (width) were imaged by manually pulling back a circumferential scanning probe along the human tongue and buccal mucosa [21]. While promising in visualizing tissue morphology, this approach is difficult to provide the information about blood perfusion. However, it is known that the microcirculation supports many vital functions [13–16]. From a clinical point of view, the importance of microcirculation is due to the fact that the capillary beds represent a vascular area where trophic-metabolic exchanges between blood and tissue take place, thus leading to an irreplaceable role in organ function [22]. In oral diagnosis, the capillary loops have long been used as clinical indicators for diseases, such as high-grade dysplasia, carcinoma in situ, systemic sclerosis, and invasive carcinoma in oral erythroplakia as compared to healthy cases [23–25]. Particularly for oral cancers and therapy-induced mucositis, the tissue vascularity is crucial in the detection of early changes for assessing the cancer margins and potentially the presence of subclinical abnormalities beyond the clinical margins [16]. Therefore, an ability to properly visualize and analyze microvascular features can be critical for improved disease staging and therapeutic management.

OCT angiography (OCTA) is a non-invasive imaging technique capable of generating 3D depth resolved vascular information using endogenous motion contrast [26]. Since the introduction of OCTA to the community of oral tissue imaging, only few works have been reported to visualize the vasculature. Being one of the OCTA variants, speckle variance OCT (svOCT) angiography has been demonstrated to delineate vasculature within labial tissue [27, 28]. Unfortunately, the microvascular network was hardly visualized, providing limited information that can quantify microvascular involvement. With the development of swept-source OCT (SS-OCT) [29], microvascular imaging of the human lip, tongue, and buccal mucosa was achieved by specifically designed forward-/side-viewing probes [30]. However, the field of view (FOV) of 2 mm × 2 mm was often too small to have useful microvascular information of diseased tissue. In clinical practices, it is necessary to evaluate microvascular network covering a FOV > 100 mm^2 [31], so that potential microvascular abnormalities can be identified over relatively large area of tissue for further examination and pathological analysis.

In this paper, we report the development of OCT based angiography system to provide 3D microcirculation information of human oral cavity over a FOV of 10 × 10 mm^2. We then demonstrate its potential by imaging ulcer lesions in the oral mucosa, a common oral mucosa disorder, penetrating into both the epithelium (EP) and lamina propria (LP) [32, 33]. Tissue morphology and vasculatures of various oral tissue sites susceptible to ulcer are also examined.

System description and data processing

For the purpose of imaging vascular features within the oral cavity tissue, we developed a swept-source OCT (SS-OCT) system to achieve OCT-based angiography with a field of view of 10 × 10 mm^2. Fig. 1a shows the schematic of the system setup, where a micro-electro-mechanical-tunable vertical cavity surface-emitting laser (VCSEL) (SL1310V1-10048, Thorlabs Inc.) was used as the swept source. The laser operates at a sweeping rate of 100 kHz over a spectral bandwidth of ~ 68 nm at a central wavelength of 1300 nm, which provided a measured axial resolution of ~ 20 μm in air. Output power of ~ 25 mW from the light source was first fiber-coupled into an OCT interferometer, where the light was split by a 90:10 fiber coupler into a sample arm and a reference arm via optical circulators. In the sample arm, there was a replaceable attenuator (attenuation coefficient of 2 dB for 1300 nm), providing an incident light power of ~ 5 mW on the sample, within the requirement of the American National Standards Institute (ANSI) standards (Z136.1) [34]. In the reference arm, an adjustable optical delay line was installed for matching optical path lengths between the reference and sample arms. Reflected lights from the reference and the sample arms were recombined at a 50/50 fiber coupler, and then detected by a 1.6 GHz balanced photodetector (PDB480C-AC, Thorlabs Inc.). The spectral interference signal was sampled and digitized by a 12 bits A/D acquisition card (ATS9350, Alazartech) with a sampling rate of 500 Ms/s. At this sampling rate, the system provided an axial ranging distance of ~ 12 mm, necessary for imaging the oral cavity where the tissue surface is typically un-even. The system sensitivity was measured at ~ 105 dB at the depth of focus. In addition, an auxiliary 635-nm aiming laser (S1FC635PM, Thorlabs Inc.) was used in the system, providing a visual guidance during imaging procedure.

The sample arm was terminated with a custom-made hand-held probe (as shown in Fig. 1b) consisting of three main parts: (1) a mounted X-Y galvanometric scanner set (Thorlabs Inc) with scanning capable of 80° angle, (2) a 50-mm achromatic doublet objective lens (AC254-050-C, Thorlabs Inc.), and (3) a disposable sample spacer to keep a constant distance between the scan lens and the sample. At the top of the spacer, a plastic head with a removable cover glass plate (diameter Φ = 15 mm) in the middle was attached in order to gently press the soft tissue within the oral cavity. Apart from the probe itself, a 3D rotation arm and a 2D

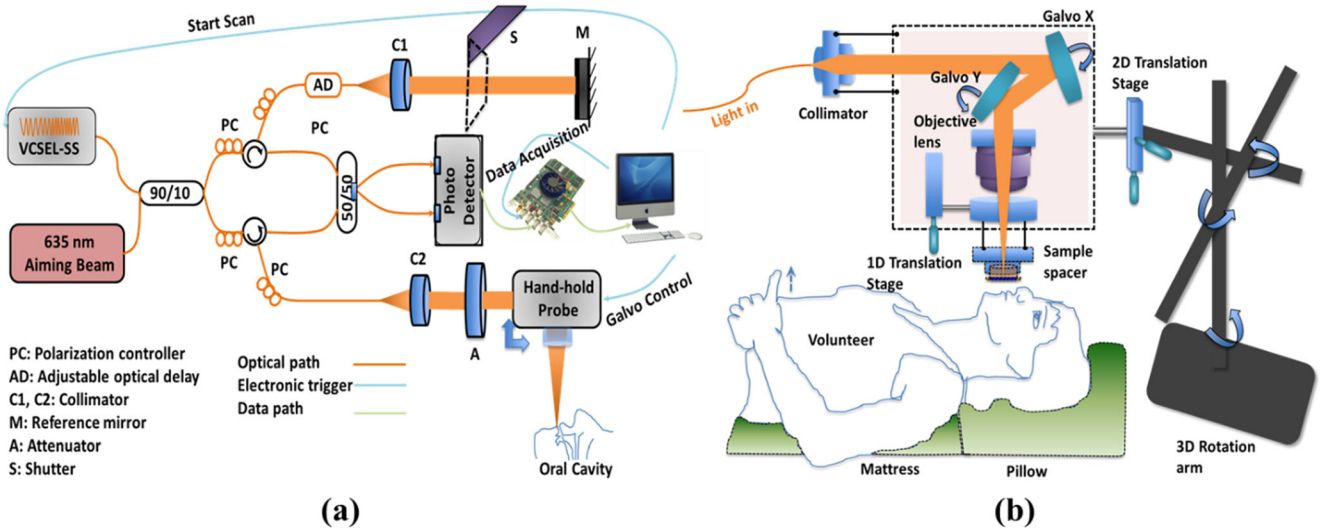

Fig. 1 **a** Schematic of the SS-OCT system setup where the sample arm is terminated with a hand-made handheld probe **b** for wide-field OCTA imaging of human oral cavity

translation stage were combined together for steadily positioning and adjusting the handheld probe.

To make full use of the temporal sensitivity in OCTA, OMAG scanning protocol was adopted [35]. We designed two separate scanning modes so that the system can provide wide-field (10 × 10 mm^2) and smaller field (5 × 5 mm^2) OCTA imaging of the oral lesions (targeted region of interest). In the first scanning mode, fast B-scan (x-direction) was 5 times repeated at 500 spatial locations along the slow axis (y-direction), which took about 12 s in total to complete one 3D scan. Each B-scan contained 500 A-scans and the scanned tissue area covered 10 mm (x) × 10 mm (y). This scanning mode provided spatial separation of 20.0 μm between adjacent A-scans and B-scans, respectively. In the second scanning mode, the 3D data acquisition format was 400 A-scans × 400 B-positions × 5 repetitions, which covered a field of view of 5 mm × 5 mm, taking about 8 s to acquire. The spacing between adjacent A-scans and B-scans was 12.5 μm.

In order to minimize the tissue motion artifacts, we co-registered the repeated B-frames at the same spatial position through a subpixel image registration algorithm [36]. Then, blood perfusion in the vessels was contrasted with five ensemble B-scans for each spatial location, which was achieved by separating dynamic scattering components from the surrounding static tissue scattering components using optical microangiography (OMAG) algorithm [37, 38]. After OMAG computation, the resulting 500 OCTA cross-sections were aligned with respect to the bottom surface of the cover glass for ease of vessel network analysis. In the analysis, we investigated the capillary loop density (the number of capillary loops per millimeter square (mm^2)) located within the papillary tissue layer, which is indicative of tissue vascularity [16, 39] and widely used in the assessment of oral diseases [22–25, 40, 41]. A user-guided segmentation software [42] was used to segment the connective tissue papillae at depth of 50~100 μm from the mucosal surface to produce enface projection (maximum intensity projection (MIP)) of microvascular network, upon which the capillary loops were counted and the density was calculated.

The in vivo imaging study that uses home-built systems to image human subjects was reviewed and approved by the Institutional Review Board of University of Washington, and the informed consent was obtained from all subjects before imaging. This study followed the tenets of the Declaration of Helsinki and was conducted in compliance with the Health Insurance Portability and Accountability Act.

Results

To demonstrate the wide-field imaging of human oral cavity, the OCT/OMAG imaging was performed on two healthy volunteers, and one subject with ulcer lesions on the labial mucosa over 2 weeks. Prior to data acquisition, the subjects rinsed their mouth with water, and then lay down on a mattress (supine position) for 10 min to acclimatize the environment (Fig. 1b). The ambient temperature and illumination were a room temperature of ~23 °C and ~ 50 lx, respectively. The probe spacer attachment was gently in contact with the tissue to be scanned, which was kept during the imaging. The attachment was replaced with new ones after each measurement. The OCT instrumentation for investigational use to image human subjects was approved by the Institutional Review Board (IRB) of University of Washington, and the informed consent was obtained from all subjects before imaging. This pilot study followed the tenets of the Declaration of Helsinki and was conducted in compliance with the Health Insurance Portability and Accountability Act.

In vivo OCT/OMAG imaging of healthy human oral mucosal tissue

Figure 2a shows a photograph of the lower lip of a healthy male volunteer (27-year-old), where the scan area (10 mm × 10 mm) was marked as a yellow box. An x-y *en face* OCT image of the scanned area (the box in Fig. 2a) is shown in Fig. 2b, in which a horizontal dotted line indicates representative cross-sectional (x-z) OCT structure image and corresponding OMAG blood flow image shown in Fig. 2c, d, respectively. No keratinization was visualized in the EP, agreeing well with the normal histology described in the standard text book. In Fig. 2c, the EP layer and underlying LP layer are clearly demarcated by a thin basement membrane (BM). It is known that the LP is a fibrous connective tissue layer consisting of a network of collagen and elastin fibers. The LP is further divided into two sub-layers: papillary and reticular layers that are differed from loose/dense connection of the fibroblasts (corresponding to low/high OCT signal intensities in Fig. 2c). Figure 2d shows superficial plexuses (SP) situated within the lamina propria that supply nutrients and oxygen for all the mucosa layers, as well as capillaries (CL) into the connective tissue papillae (the interdigitations from the lamina propria into the epithelium). In Fig. 2e, an x-y *en face* OCT angiogram (10 mm × 10 mm) of the 3D OMAG image dataset delineates a capillary network within the labial mucosa, in which the capillary loops are concentrated, originating from but approximately normal to the underlying vascular plexus in the LP. The LP plexus could be more clearly identified from the deeper reticular layer (RL) as Fig. 2f, giving an appearance of the big vessel limbs (VL) and their small branches (VB). Figure 2g shows volume-rendered representation of the fused OCT-OMAG image dataset.

In vivo OCT/OMAG imaging of human oral mucosal tissue affected by ulcer lesion

An abnormal oral mucosal tissue was imaged from a 36-year-old male volunteer suffering from recurrent minor mouth ulcer (aphthous ulcer). In Fig. 3a, a photograph shows the mouth ulcer on the labial mucosa at day 7 after occurrence, which can also be identified in the 10 mm × 10 mm OCT *en face* image in Fig. 3b. The ulcer was appeared as small, ovoid, highly reflective tissue breaking with circumscribed margins (erythematous halo). Cross-sectional (x-z) OCT structure image and corresponding OMAG blood flow image are shown in Fig. 3c, d, respectively, which were extracted at a location crossing the ulcer center (horizontal line in Fig. 3b–f). Interestingly, it was observed a slough-like perforation in the ulcer with cornered hyper-reflective spots (red arrows) visible in Fig. 3c. Presence of the scatters is believed to be dead cells or their clusters as a result of the process of phagocytosis at inflammation stage [43]. It can be explained that the mouth ulceration induces the disintegration and necrosis of the EP layer due to lymphocyte-mediated immune response that involves the generation of interleukins and tumor necrosis factor alpha (TNF-α) to regulate the immune cells [44]. Note that such scatters are still present in the OMAG image (Fig. 3d), which means that OMAG is sensitive enough to detect the slow motion of the scatters floating in the ulcer space. In the capillary network of the papillary layer (Fig. 3e) and the underlying vessel network in the reticular layer (Fig. 3f), substantial loss of the capillary loops is apparent in the perforated ulcer but rather less at the superficial vascular plexuses beneath the ulcer. The volume rendered representation of the fused OCT-OMAG image dataset is displayed in Fig. 3g.

At day 11 after ulcer occurrence, OCT/OMAG images show significant self-healing of the ulcer lesion at proliferation stage without any medical intervention, including contraction of the lesion site and concurrently re-epithelialization of the EP layer, and formation of new vessels in the ulcer lesion as shown in Fig. 4a–g. The volume rendered representation of fused OCT-OMAG image dataset is displayed in Fig. 4g. In Figs. 3 and 4, all ulcer regions in the OCT/OMAG images are marked in yellow squares.

In vivo OCT/OMAG imaging of mouth ulcer progression

In order to observe the mouth ulcer progression, we monitored from the ulcer formation to its natural recovery. For this investigation, the imaging range was reduced to 5 mm × 5 mm FOV, which provided a closer view of the imaging area into the ulcer. Figure 5 depicts structural and vascular changes in the ulcer at different time points: (Fig. 5(a.1–8)): x-y *en face* OCT views of the structures, (Fig. 5(b.1–8)): the corresponding x-y *en face* OMAG views of the vasculatures, (Fig. 5(c.1–8)): the representative cross-sectional (x-z) OCT structure images, (Fig. 5(d.1–8)): the corresponding cross-sectional (x-z) OMAG blood flow images. The figures with numbers (#1–8) were obtained at day 1, day 3, day 5, day 7, day 9, day 11, day 13, and day 15 following ulcer occurrence, respectively. From Fig. 5(a.1, a.2), we can see the superficial erosion of the EP layer. In day 3 (Fig. 5(b.2)), few vessels (green arrows) were observed in the ulcer region. It is probably because of an air bubble trapped between the ulcer and the cover glass, acting like a singlet lens (RI of the air bubble is smaller than the tissue region of interest) to focus the probe beam into deeper layer. In Fig. 5(b.1–2, d.1–2), there are strong OMAG signals across the lesion (see the regions between yellow dashed circles), which is probably because interstitial fluids containing immune cells flew into the ulcer following the onset of inflammation [45]. This is evidenced from the fact that early stage of the aphthous ulcer is featured with dense inflammatory infiltration with 80% constituted of T lymphocytes [46]. On day 5, however, the inflammation-

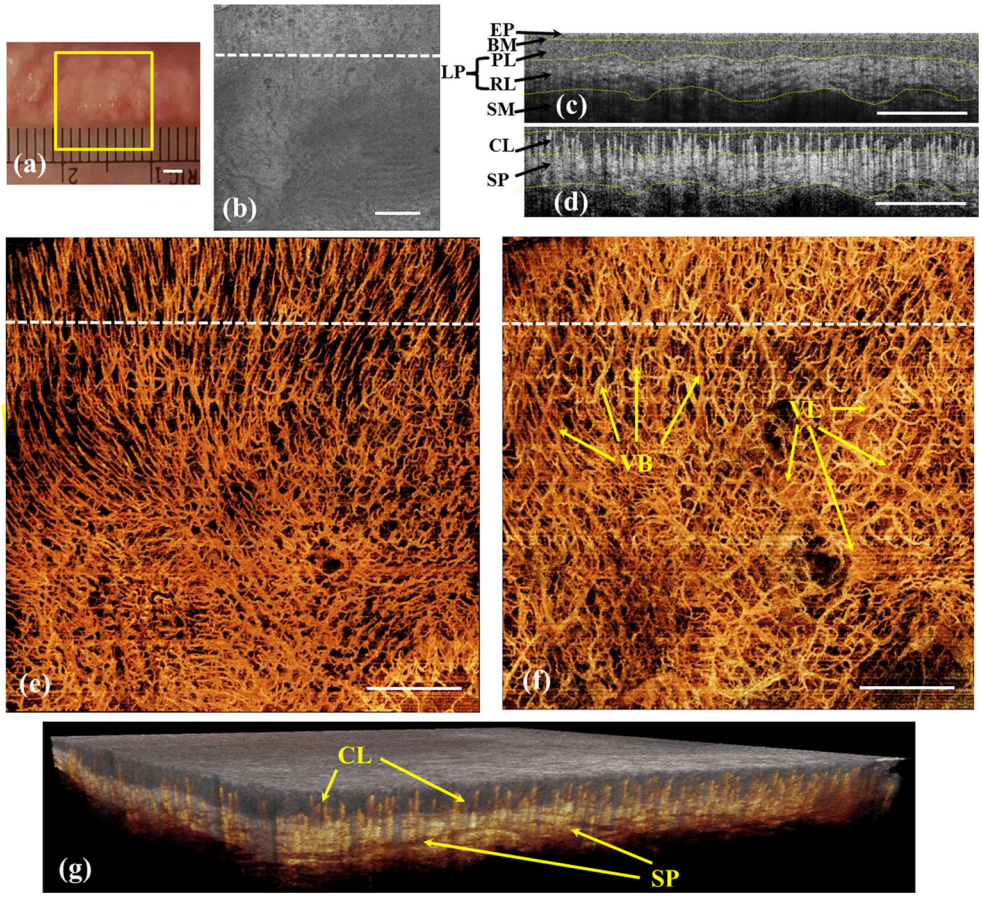

Fig. 2 In vivo 10 × 10 mm^2 FOV OCT/OMAG images of healthy labial mucosa. **a** Photograph of the labial mucosa tissue of the lower lip with a metric ruler indicating the scanned FOV, and **b** OCT MIP (x-y) image (10 mm × 10 mm) of the mucosa structure marked as a yellow square in (**a**). **c** Representative OCT cross-section (x-z) and **d** corresponding OMAG cross-section (x-z) at a location marked by the horizontal dotted line in (**b**), (**e**), and (**f**), respectively. **e** and **f** are OMAG MIP (x-y) images (10 mm × 10 mm) showing dense superficial capillary loops in the papillary layer and vascular plexus sited in the reticular layer, respectively. **b** Volume rendered representation of fused structure (gray) and vasculature (yellow) image dataset. The yellow dashed curves in (**c**) and (**d**) are segmentation boundaries used to separate different mucosa layers, i.e., EP: epithelium, BM: basement membrane, PL: papillary layer, RL: reticular layer, and SM: submucosa. LP: lamina propria includes both PL and RL. VL and VB are the vessel limbs and vessel branches of the superficial plexuses network. CL: capillary loop and SP: superficial plexuses. Scale bars 2 mm

induced OMAG signal was totally diminished whereas the most of blood vessels below the ulcer are disappeared as shown in Fig. 5(b.3, d.3). The images at day 7, where the ulceration would be in active, have been previously shown in Fig. 3 in the "In vivo OCT/OMAG imaging of human oral mucosal tissue affected by ulcer lesion" section. Unlike Fig. 3d, dead cells or their clusters are not visible in Fig. 5(d.4). This might be due to the faster B-frame rate (200 fps) for 5 mm × 5 mm imaging mode than that of 10 mm × 10 mm imaging mode (160 fps), which makes the former one relatively less sensitive to detect the cells very slowly moving in the blister. After that, the ulcer perforation was closed and the lesion in LP layer was almost restored through 1 week wound healing (from day 9 to day 15) as shown in the OCT/OMAG results (Fig. 5(a–d.5 to a–d.8). However, the epithelium layer still needed one more week for fully recovery (not shown here).

Ulcer development evaluation based on capillary loop density quantification

It is known that the mucosa capillary loops are easily affected by oral diseases and its population is associated with the disease progression [47]. In order to determine if the changes in the capillary loop population could be identified and quantified on OCTA images [48], we counted individual capillary loops normal to the oral tissue surface, appearing as regularly distributed dots or commas in the enface OMAG images. To count the capillary loops, the connective tissue papillae (~50 μm in thickness) was segmented from the OMAG volume dataset. Figure 6(a.1–8) show OCTA angiograms of the segmented papillae layers at each day, depicting the well-resolved individual capillary loops. In Fig. 6(a.8), the vascularization (red arrows) shows active wound healing at the proliferation stage. The

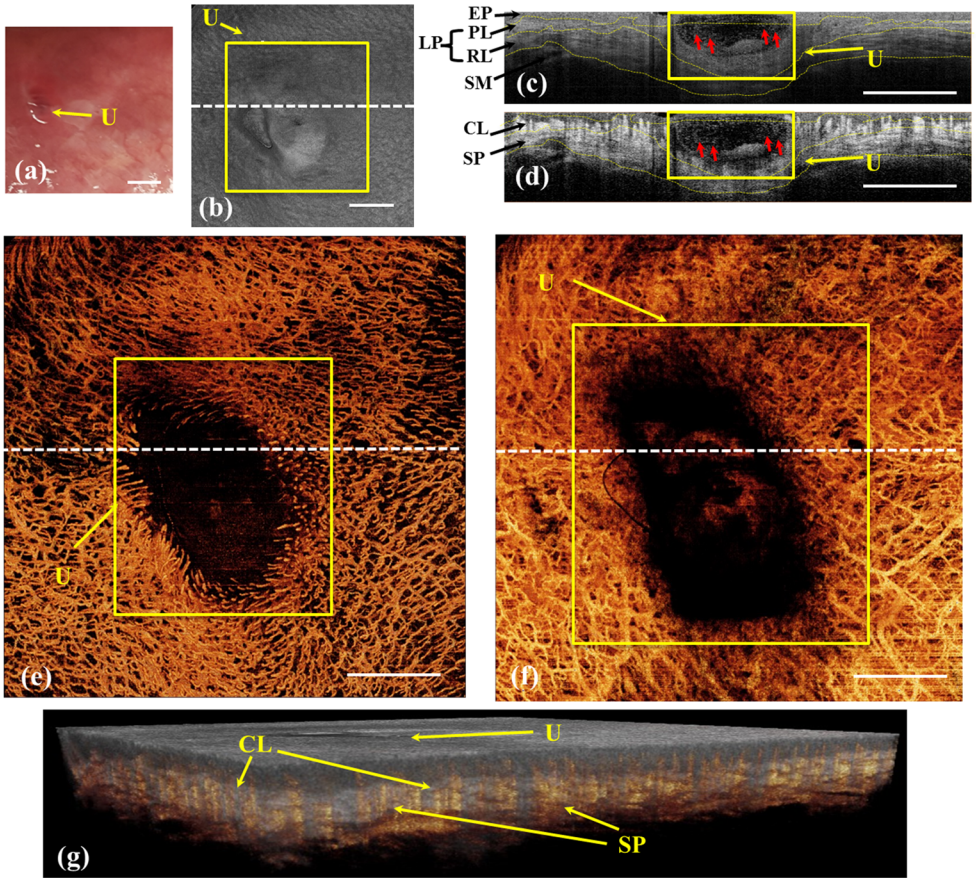

Fig. 3 In vivo 10 × 10 mm^2 FOV OCT/OMAG images of labial mucosa with a mouth ulcer at day 7 after occurrence **a** Photograph of the mucosa tissue of the lower lip with the ulcer (U), and **b** OCT MIP (x-y) image of the ulcer-affected region. **c** Representative OCT cross-section (x-z) and **d** corresponding OMAG cross-section (x-z) at the location marked by a horizontal dotted line in (**b**), (**e**), and (**f**), respectively, showing floating scatters (indicated by red arrows) in slow motion inside the ulcer perforation. **e** and **f** are OMAG MIP (x-y) images (10 mm × 10 mm) of the micro-vasculature within the papillary layer and within the reticular layer, respectively. **g** Volume rendered representation of fused structure (gray) and vasculature (yellow) image dataset. The yellow dashed curves in (**c**) and (**d**) are segmentation boundaries for dividing mucosa layers, i.e., EP: epithelium, PL: papillary layer, RL: reticular layer, and SM: submucosa. LP: lamina propria includes both PL and RL. U: ulcer, CL: capillary loop, and SP: superficial plexuses. Scale bars 2 mm

capillary loops in an annular area at a given distance (2.25 to 3.5 mm) to the ulcer center were manually counted and its density (counts/mm^2) was calculated on each day. The manual counting was repeated for 5 times by 5 masked individuals to avoid the influence of subjectivity. Additionally, capillary loops in the ulcer-free region contralateral to the lesion were also measured from the same subject on the same day as a control. Figure 6b shows changes in the capillary loop density in the healthy (red line) and ulcer regions (blue line) of the subject. It was surprising that from initiation of ulcer (day 1), the capillary loop density was dramatically increased above the healthy ones, and then declined to the same level at day 15. This trend was quite different from the healthy ones that remained almost the same throughout the period of 2 weeks. The elevation of surrounding capillary loop density may represent an interesting finding that deserves further mechanistic investigation. The finding for healthy ones is in good agreement with previous results using microscopy [40] .

In vivo OCT/OMAG imaging of different human oral cavity tissues

There are various ulcer-susceptible sites in the human oral cavity, involving labial mucosa, tongue, gingivae, alveolar mucosa, and labial frenulum. To further demonstrate the imaging flexibility of our instrument, we imaged the tongue, lower labial frenulum, and upper labial frenulum of another healthy volunteer (28-year-old male). The photographs (Fig. 7(a.1–3), the corresponding 3D-rendered OCT structures (Fig. 7(b.1–3), the OCT angiograms (Fig. 7(c.1–3), the cross-sectional structure images (Fig. 7(d.1–3)), and the cross-sectional blood flow images (Fig. 7(e.1–3) of the tip of the upper tongue, lower labial

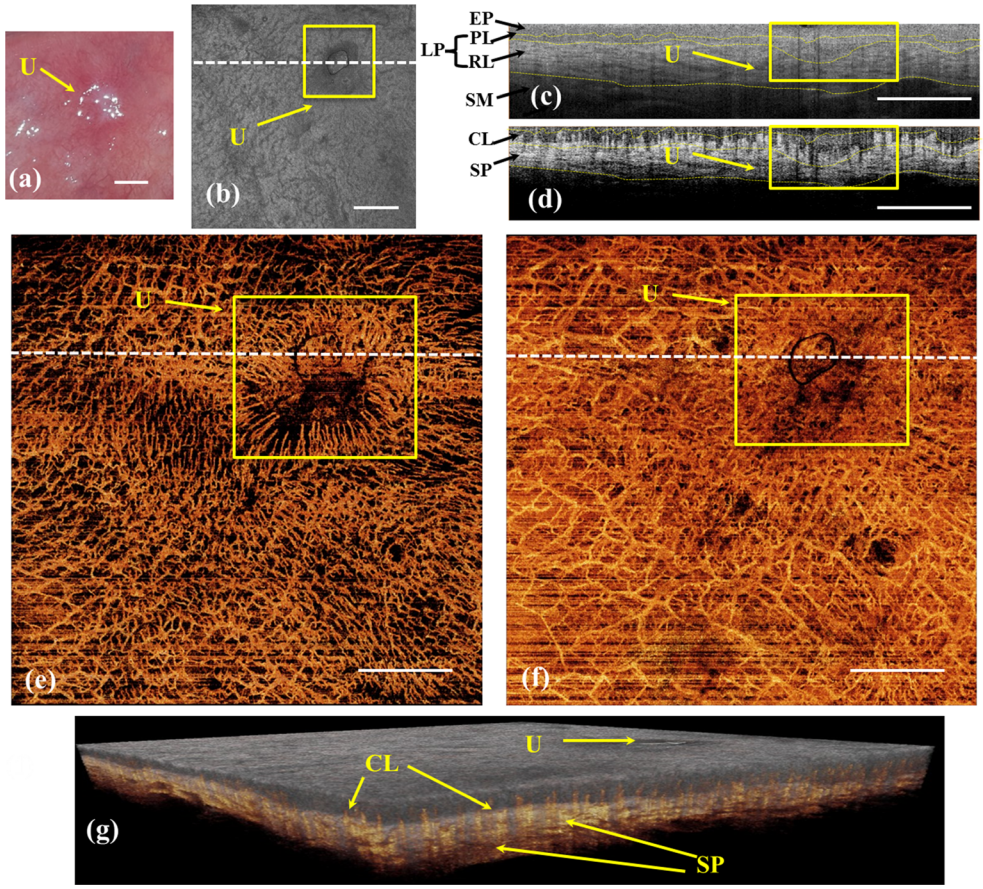

Fig. 4 In vivo 10 × 10 mm^2 FOV OCT/OMAG images of labial mucosa with the mouth ulcer at day 11 after occurrence. **a** Photograph of the mucosa tissue of the lower lip with the ulcer (U). **b** Corresponding OCT MIP (x-y) image showing mucosa surface in recovery. **c** Representative OCT cross-section (x-z) and (d) corresponding OMAG cross-section (x-z) at a location marked by a horizontal dotted line in (**b**), (**e**), and (**f**) respectively. **e** and **f** are OMAG MIP (x-y) images (10 mm × 10 mm) of the micro-vasculature within the papillary layer and within the reticular layer, respectively. **g** Volume rendered representation of fused structure (gray) and vasculature (yellow) image dataset. The yellow dashed curves in (**c**) and (**d**) are segmentation boundaries for dividing mucosa layers, i.e., EP: epithelium, PL: papillary layer, RL: reticular layer, and SM: submucosa. LP: lamina propria includes both PL and RL. U: ulcer, CL: capillary loop, and SP: superficial plexuses. Scale bars 2 mm

frenulum, and upper labial frenulum are displayed, respectively.

The tongue plays many important roles in the digestive system and is the primary organ of taste in the gustatory system, as well as provides air-conditioning function when breathing through the mouth, which all require sufficient blood supply [49]. As shown in Fig. 7(b.1) the rough upper surface of the tongue is depicted as the raised protrusions called lingual papillae. In the vascular appearance of Fig. 7(c.1, e.1), two types of the lingual papillae are identified: the wide mushroom-shaped fungiform papillae (Fungi) and the thin long conical-shaped filiform papillae (Fili). As the taste buds accumulated at the surface of the fungiform papillae to sense the five tastes, salts, bitter, sweet, sour, and umami [50], abundant capillary loops are formed in the fungiform papillae appearing like blooming flowers, while less capillaries are in the filiform papillae as they are not involved in the gustation [51].

During oral examination, dentists usually pay little attention to the frenulum; however, an abnormal frenulum can be indicators of various oral syndromes [52]. For example, papillary and papilla penetrating frena have been found in association with loss of papilla, recession, diastema, difficulty in brushing, malalignment of teeth, et al. [53]. The abnormal frenulum may also prejudice the denture fit or retention that leading to psychological disturbances to the patients [53]. In traditional approach, abnormal or aberrant frena are detected visually, by applying tension over them to see the movement of papillary tip or blanching due to ischemia of this region, which however largely depends on the medical experience and subjective criteria of the examiners. These downsides may be easily overcome by our OCT/OMAG system. To image the rugged lower labial frenulum, we removed the sample spacer of the probe head. Abundant capillary vessels in the lower frenulum and alveolar mucosa are identified as shown in Fig. 7(c.2) with small amount of attached gingivae

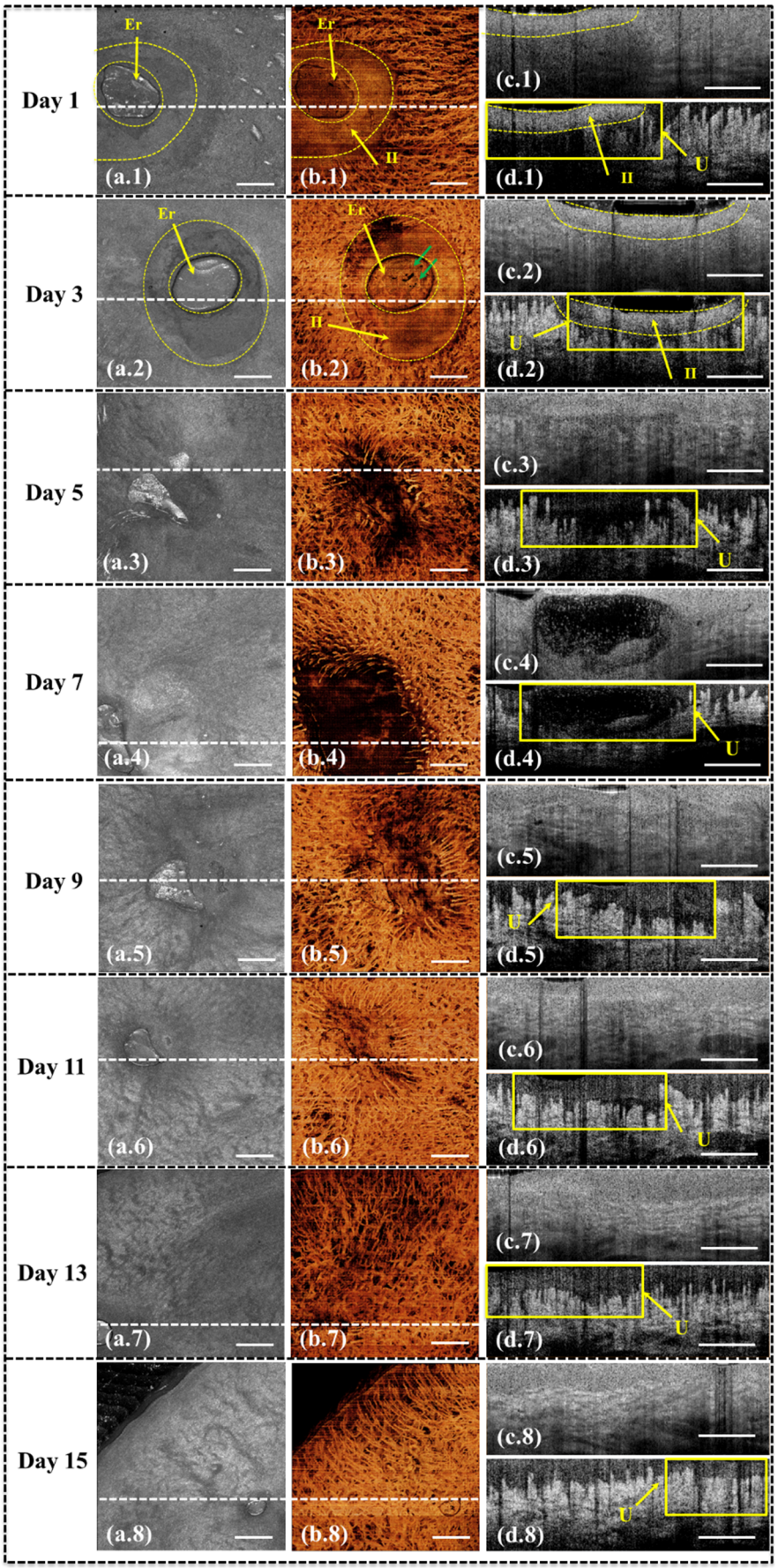

Fig. 5 In vivo 5 × 5 mm^2 FOV OCT/OMAG images for evaluation of ulcer lesion recovery over a period of 2 weeks. (a.1~a.8) *en face* views of the labial tissue structure and (b.1~b.8) corresponding vasculature, in which white dashed lines indicate (c.1~c.8) cross-sectional structure images and (d.1~d.8) blood flow images across the ulcer lesion. Figure numbers # 1~8 correspond to the results of day 1, day 3, day 5, day 7, day 9, day 11, day 13, and day 15. Er: erosion, U: ulcer, and II: inflammatory infiltration. In (b.2), deeper vessels in the ulcer region are indicated by green arrows. Scale bars 1 mm

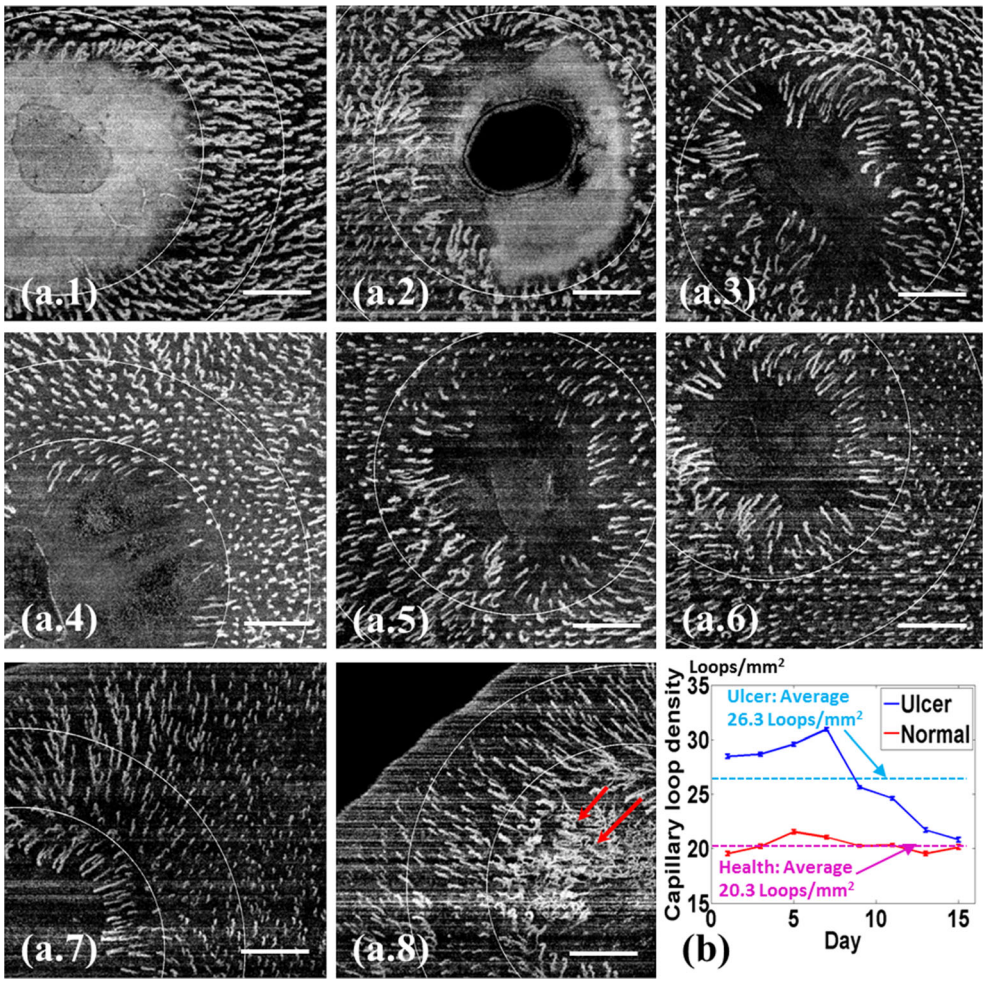

Fig. 6 (a.1~a.8) OMAG mean intensity projections of the superficial papillary layer for quantitative evaluation of ulcer development through the measurement of capillary loop density. Regions of interest (ROI) for quantification are indicated between white arc lines. Scale bars: 1 mm. (b) Variations of capillary loop density per mm^2 in the region affected by aphthous ulcer (blue line) and in the contralateral healthy region (red line) along the recovery timeline. The capillary density for healthy labial mucosa tissue is ~ 20.3 Loops/mm^2. In comparison, the capillary density for ulcer-affected tissue is ~ 26.3 Loops/mm^2. In (a.8), the intensive vascularization is indicated by red arrows. All quantification error bars are < 5%

capillaries at the left corner (red arrows), showing impressive clinical findings.

Sometimes, an upper frenulum causes significant problem because tension from lip movement pulls the gingival margin away from the tooth, or the frenulum tissue inhibits the closure of a diastema during orthodontic treatment [53]. A labial frenectomy surgery is usually manipulated to remove the overgrown labial frenulum in order to release the tension or open the inhibition [54]. OCT-based angiography can be an invaluable tool to identify the frenulum abnormalities, analyze the orthodontic surgery, and avoid recrudesce. Figure 7(c.3) shows leaf-vein-like capillary vessel distribution on the upper lip that is clearly influenced by the frenulum.

Discussion and conclusion

In this study, we have demonstrated OCT angiography (OCTA) of human oral cavity in vivo with a field of view of 100 mm^2. We have shown its potential application for examining ulcer lesions on labial tissues, where the OCT angiograms (100 mm^2) have provided visualization of micro-scale vessel network in the ulcer site. Time-course monitoring of the ulcer has found that the alteration in vessel network was closely involved with the ulcer development and recovery. Although we demonstrated a field of view at 10 × 10 mm^2, the practical clinical application may still require even larger field of view. Recently, OCTA imaging of the human nailfold has been achieved up to 750 mm^2 by using a spectral domain OCT (SD-OCT) with wide-scanning optics [31]. It is foreseeable that the future development of swept-source OCT/OCTA can provide wider field of view imaging for oral cavity for the following reasons: (1) the development of swept laser source has been rapid, with a recent report that demonstrated a sweeping rate at 20 MHz [55]; and (2) swept-source OCT is capable of high sensitivity and long ranging distance, which attributes are important for oral cavity imaging because the tissue surface is highly un-even.

According to the statistical investigation in [40] on 45 healthy subjects, the average size of capillary loops in oral cavity is about 32 μm with 9 μm in diameter for incoming branch (connected with arteriole) and 14 μm for outgoing branch (connected with venule). In our system, the objective lens with a focal length of 50 mm provided a theoretical beam

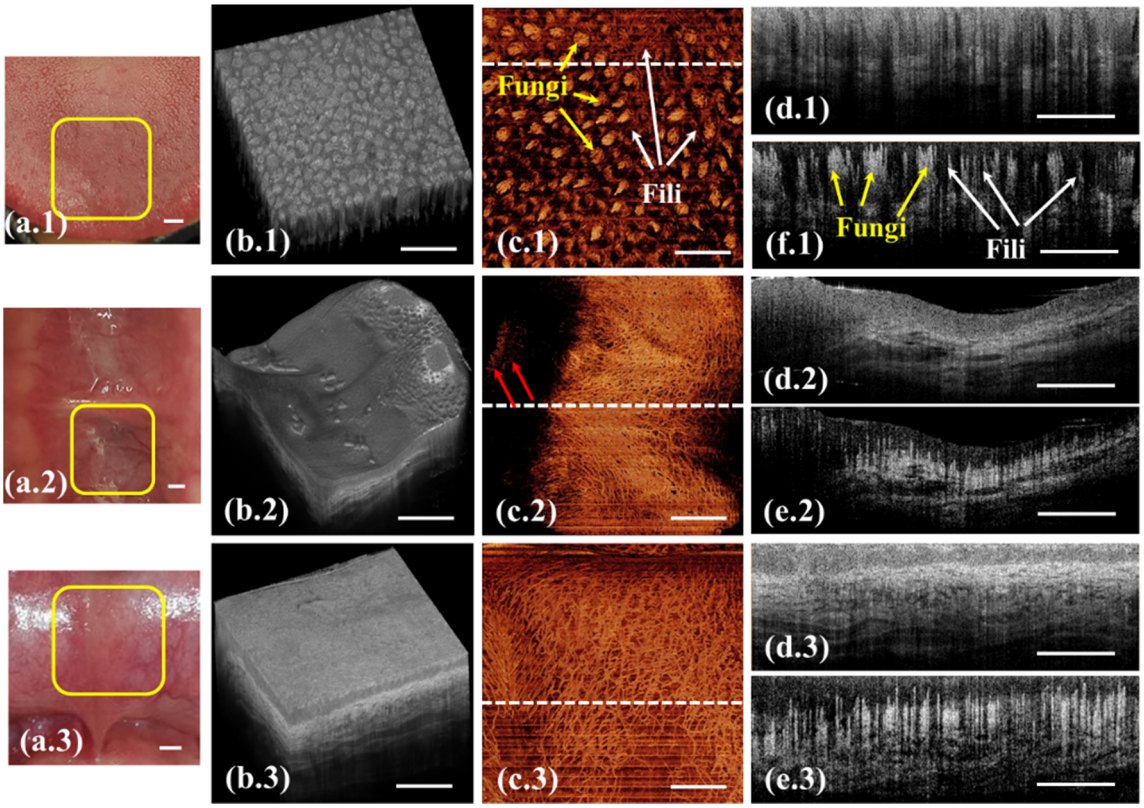

Fig. 7 In vivo 10 × 10 mm^2 FOV OCT/OMAG imaging of various tissue beds in human oral cavity. (a.1~a.3) Photographs of the upper tongue tip, lower labial frenulum, and upper labial frenulum, respectively, in which yellow boxes indicate the scanning FOV. (b.1~b.3) 3D rendered tissue structures and (c.1~c.3) corresponding OMAG MIP views of the vasculatures, in which white dashed lines indicate (d.1~d.3) cross-sectional structure images and (e.1~e.3) corresponding blood flow images, respectively. In (c.1) and (f.1), capillary loops in fungiform papillae (Fungi) and filiform papillae (Fili) are indicated by yellow arrows and white arrows, respectively. In (c.2), gingivae capillaries are indicated by red arrows. Scale bars: 2 mm

size of 17 μm at FWHM. Combined with the lateral spacing of 12.5 μm for 5 mm × 5 mm FOV, the total capillary loops can be easily distinguished for precise density analysis. While, single branches are still indivisible that need more efforts on lens' designs to involve in more quantitative parameters like capillary diameter and capillary length.

The vascularization could be clearly visualized during the ulcer healing process, especially at the proliferation stage (see Fig. 6(a.8). Angiogenesis is a crucial process in the wound healing that is regulated by the chemotactic response of vascular endothelial cells to macrophage-derived factors produced in the wound space [56]. The difficulty in studying the angiogenesis is in the lack of tools for measuring angiogenic activity in vivo. A commonly used method is to measure the vessel density in histological sections of biopsy at end point [41]. OCTA and capillary analysis used in this work would be able to provide quantitative information about the angiogenesis at the viable state, ensuring accuracy and reliability in the evaluation of wound healing process. To improve the manual counting of capillary loops, we are currently working on the automation of capillary density grading which would be beneficial for oral diseases assessment in clinic.

While the present work is promising, there are some issues remaining to be addressed. First, the optics in handheld probe has not been well optimized. The current off-the-shelf achromatic doublet lens has limitation in wide-field laser-scanning application due to its observed curved image plane. At scanning angles larger than a given degree (e.g., 80°), it would introduce spherical aberrations. Besides, when using a broadband light source, the chromatic aberrations resulting from the dispersion would induce array of foci of different light wavelengths on optical axis. In the current system, the maximum focal shift by the Thorlabs AC254-050-C achromatic doublet is calculated to be ~45 μm for a 68 nm spectral bandwidth of light source. These issues may be solved by using a custom-designed aberration-free objective lens or adaptive optics. Second, although the depth range of 12 mm is enough to image the oral tissues, sometimes there are still limitations for imaging the physically complex and deep-located structures like the frenum of the tongue or the circumvallate papillae on the tongue. In the next work, we are planning to adopt a 4.0 Gs/s digitizer in place of the current 500 Ms/s one, which can make full use of the 1.6 GHz bandwidth of the photodetector and provide a theoretical depth range of ~90 mm, sufficient for imaging those oral sites.

In conclusion, we have presented microvascular imaging of oral cavity tissues in vivo with OCT angiography technology. The imaging performance of the achieved OCTA has been tested and validated by imaging, monitoring, and quantifying the micro-vessels in the mouth ulcer lesions and various candidate tissue sites of oral diseases within a FOV of 100 mm^2. Technical optimization of the presented OCT angiography approach may promise a clinical application in the not too distant future.

Funding source and its role in the study This work was supported in part by research grants from the National Heart, Lung, and Blood Institute (R01 HL093140). The content is solely the responsibility of the authors and does not necessarily represent the official views of grant giving bodies.

Compliance with ethical standards

Conflict of interest The authors declare that they have no conflict of interest.

Ethical approval The in vivo imaging study that uses home-built systems to image human subjects was reviewed and approved by the Institutional Review Board of University of Washington, and the informed written consent was obtained from all subjects before imaging. This study followed the tenets of the Declaration of Helsinki and was conducted in compliance with the Health Insurance Portability and Accountability Act.

Reference

1. American Cancer Society (2017) Cancer Facts & Figures 2017. American Cancer Society, Atlanta
2. American Cancer Society (2015) Global Cancer Facts & Figures 3rd Edition. American Cancer Society, Atlanta
3. National Cancer Institute (2011) Cancer Statistics Review 1975–2011: Introduction. https://seer.cancer.gov/archive/csr/1975_2011/results_merged/sect_01_overview.pdf
4. Squier CA, Kremer MJ (2001) Biology of oral mucosa and esophagus. J Natl Cancer Inst Monogr 29:7–15
5. Maher NG et al (2016) In vivo confocal microscopy for the oral cavity: current state of the field and future potential. Oral Oncol 54: 28–35
6. Muldoon TJ et al (2012) Noninvasive imaging of oral neoplasia with a high-resolution fiber-optic microendoscope. Head Neck 34(3):305–312
7. Xu MH, Wang LHV (2006) Photoacoustic imaging in biomedicine. Rev Sci Instrum 77(4):041101. https://doi.org/10.1063/1.2195024
8. Tomlins PH, Wang RK (2005) Theory, developments and applications of optical coherence tomography. J Phys D Appl Phys 38(15): 2519–2535
9. Fercher AF et al (2003) Optical coherence tomography-principles and applications. Rep Prog Phys 66(2):239
10. Drexler W and Fujimoto JG (2008) Optical coherence tomography: technology and applications. Springer Science & Business Media. Berlin
11. Muanza TM et al (2005) Evaluation of radiation-induced oral mucositis by optical coherence tomography. Clin Cancer Res 11(14): 5121–5127
12. Kawakami-Wong H et al (2007) In vivo optical coherence tomography-based scoring of oral mucositis in human subjects: a pilot study. J Biomed Opt 12(5):051702
13. Tsai MT et al (2008) Effective indicators for diagnosis of oral cancer using optical coherence tomography. Opt Express 16(20):15847–15862
14. Wilder-Smith P et al (2009) In vivo diagnosis of oral dysplasia and malignancy using optical coherence tomography: preliminary studies in 50 patients. Lasers Surg Med 41(5):353–357
15. DeCoro M, Wilder-Smith P (2010) Potential of optical coherence tomography for early diagnosis of oral malignancies. Expert Rev Anticancer Ther 10(3):321–329
16. Wilder-Smith P et al (2010) Optical diagnostics in the oral cavity: an overview. Oral Dis 16(8):717–728
17. Motamedi S et al (2011) Gold nanorods for intravital vascular imaging of preneoplastic oral mucosa. Biomed Opt Express 2(5): 1194–1203
18. Gladkova N et al (2013) Evaluation of oral mucosa collagen condition with cross-polarization optical coherence tomography. J Biophotonics 6(4):321–329
19. Lee CK et al (2012) Diagnosis of oral precancer with optical coherence tomography. Biomed Opt Express 3(7):1632–1646
20. Grulkowski I et al (2013) Quantitative assessment of oral mucosa and labial minor salivary glands in patients with Sjogren's syndrome using swept source OCT. Biomed Opt Express 5(1):259–274
21. Lee AM et al (2015) Wide-field in vivo oral OCT imaging. Biomed Opt Express 6(7):2664–2674
22. Scardina GA, Messina P (2009) Morphological characteristics of microcirculation in oral lichen planus involving the lateral border of the tongue. J Oral Sci 51(2):193–197
23. Grassi W et al (1993) Labial capillary microscopy in systemic sclerosis. Ann Rheum Dis 52(8):564–569
24. Yang SW et al (2015) Clinical characteristics of narrow-band imaging of oral erythroplakia and its correlation with pathology. BMC Cancer 15:406
25. Scardina GA, Fuca G, Messina P (2007) Microvascular characteristics of the human interdental papilla. Anat Histol Embryol 36(4): 266–268
26. Zhang A et al (2015) Methods and algorithms for optical coherence tomography-based angiography: a review and comparison. J Biomed Opt 20(10):100901
27. Davoudi B et al (2012) Noninvasive in vivo structural and vascular imaging of human oral tissues with spectral domain optical coherence tomography. Biomed Opt Express 3(5):826–839
28. Davoudi B et al (2013) Optical coherence tomography platform for microvascular imaging and quantification: initial experience in late oral radiation toxicity patients. J Biomed Opt 18(7):76008
29. Tsai MT et al (2008) Delineation of an oral cancer lesion with swept-source optical coherence tomography. J Biomed Opt 13(4): 044012
30. Choi WJ, Wang RK (2014) In vivo imaging of functional microvasculature within tissue beds of oral and nasal cavities by swept-source optical coherence tomography with a forward/side-viewing probe. Biomed Opt Express 5(8):2620–2634
31. Xu J et al (2016) Scalable wide-field optical coherence tomography-based angiography for in vivo imaging applications. Biomed Opt Express 7(5):1905–1919
32. Dziedzic A, Wiench R (2015) Ulceration: More on aphthous ulceration. Br Dent J 218(12):663
33. Rogers RS III (1992) Common lesions of the oral mucosa. A guide to diseases of the lips, cheeks, tongue, and gingivae. Postgrad Med 91(6):141–148, 151–143
34. Bauman N (1989) ANSI (American National Standards Institute) laser standard: no easy answers for tough questions. OR Manager 5(1):1, 6-7

35. Wang RK et al (2010) Depth-resolved imaging of capillary networks in retina and choroid using ultrahigh sensitive optical microangiography. Opt Lett 35(9):1467–1469
36. Guizar-Sicairos M, Thurman ST, Fienup JR (2008) Efficient subpixel image registration algorithms. Opt Lett 33(2):156–158
37. Yousefi S, Zhi ZW, Wang RKK (2011) Eigendecomposition-based clutter filtering technique for optical microangiography. IEEE Trans Biomed Eng 58(8):2316–2323
38. An L, Qin J, Wang RK (2010) Ultrahigh sensitive optical microangiography for in vivo imaging of microcirculations within human skin tissue beds. Opt Express 18(8):8220–8228
39. Altmeyer P, Hoffmann K, el Gammal S, Hutchinson J (2012) Wound healing and skin physiology, Springer Science & Business Media. Berlin
40. Scardina GA, Cacioppo A, Messina P (2009) Anatomical evaluation of oral microcirculation: capillary characteristics associated with sex or age group. Ann Anat =Anat. Anz 191(4):371–378
41. Lova RM et al (2002) Morphologic changes in the microcirculation induced by chronic smoking habit: a videocapillaroscopic study on the human labial mucosa. Am Heart J 143(4):E2
42. Yin X, Chao JR, Wang RK (2014) User-guided segmentation for volumetric retinal optical coherence tomography images. J Biomed Opt 19(8):086020
43. Hasturk H, Kantarci A, Van Dyke TE (2012) Oral inflammatory diseases and systemic inflammation: role of the macrophage. Front Immunol 3:118
44. Brocklehurst P et al (2012) Systemic interventions for recurrent aphthous stomatitis (mouth ulcers). Cochrane Database Syst Rev 9:CD005411
45. Koch LH et al (2009) Randomized comparison of virtual microscopy and traditional glass microscopy in diagnostic accuracy among dermatology and pathology residents. Hum Pathol 40(5): 662–667
46. Neville TL et al (2008) Effects of level and source of dietary selenium on maternal and fetal body weight, visceral organ mass, cellularity estimates, and jejunal vascularity in pregnant ewe lambs. J Anim Sci 86(4):890–901
47. Scardina GA, Ruggieri A, Messina P (2009) Oral microcirculation observed in vivo by videocapillaroscopy: a review. J Oral Sci 51(1): 1–10
48. Reif R, Qin J, An L, Zhi Z, Dziennis S, Wang R (2012) Quantifying optical microangiography images obtained from a spectral domain optical coherence tomography system. Int J Biomed Imaging. https://doi.org/10.1155/2012/509783
49. Hellekant C, Kaude J (1972) Renal vein thrombosis. Radiologe 12(11):349–357
50. Arvidson K, Friberg U (1980) Human taste: response and taste bud number in fungiform papillae. Science 209(4458):807–808
51. Naumova EA et al (2013) The oral mucosal surface and blood vessels. Head Face Med 9:8
52. Kakodkar S et al (2010) Reversible cardiomyopathy in an adolescent with idiopathic aortic cusp ventricular tachycardia. Pediatr Cardiol 31(1):147–150
53. Priyanka M et al (2013) An overview of frenal attachments. J Indian Soc Periodontol 17(1):12–15
54. Medeiros Junior R et al (2015) Labial frenectomy with Nd:YAG laser and conventional surgery: a comparative study. Lasers Med Sci 30(2):851–856
55. Wieser W et al (2010) Multi-megahertz OCT: high quality 3D imaging at 20 million A-scans and 4.5 GVoxels per second. Opt Express 18(14):14685–14704
56. Arnold F, West DC (1991) Angiogenesis in wound healing. Pharmacol Ther 52(3):407–422